



1 **Improvement in algorithms for quality control of weather radar data** 2 **(RADVOL-QC system)**

3
4 Katarzyna Ośródkka¹, Jan Szturc¹

5 ¹Centre of Meteorological Modelling, Institute of Meteorology and Water Management – National Research Institute, PL 01-
6 673 Warszawa, ul. Podleśna 61, Poland

7 *Correspondence to:* Katarzyna Ośródkka (katarzyna.osrodka@imgw.pl)

8 **Abstract.** Data from weather radars are commonly used in meteorology and hydrology, but they are burdened with serious
9 disturbances, especially due to the appearance of numerous non-meteorological echoes. For this reason, these data are
10 subject to advanced quality control algorithms. The paper presents a significant improvement of the RADVOL-QC system
11 made necessary by the appearance of an increasing number of various disturbances. New algorithms are mainly addressed to
12 the occurrence of clutter caused by wind turbines (DP.TURBINE algorithm) and other terrain obstacles (DP.NMET
13 algorithm), as well as various forms of echoes caused by the interaction of a radar beam with RLAN signals (set of SPIKE
14 algorithms). The individual algorithms are based on the employment of polarimetric data as well as on the geometric
15 analysis of echo patterns. In the paper the algorithms are described along with examples of their performance and an
16 assessment of their effectiveness, and finally examples of the performance of the whole system are discussed.

17 **1. Introduction**

18 Weather radar data are widely employed in weather monitoring and forecasting, thus they have been significantly improved,
19 and observational capabilities of radars have been enhanced in response to increasing demands for better resolution and
20 accuracy. In particular, the enhancement of the accuracy of a quantitative precipitation estimation (QPE) has been a primary
21 goal in weather radar applications in meteorology and hydrology. Moreover, the upgrade to dual-polarization has promised
22 substantial improvements in data reliability since polarimetric parameters offer many opportunities by compensating for
23 various factors that cause measurement errors, such as the occurrence of different types of non-meteorological echoes,
24 especially those caused by interfering radio local area network (RLAN) signals and wind turbines (e.g., Bringi et al., 2011;
25 Saltikoff et al., 2019).

26 Radar precipitation estimates are affected by numerous sources of uncertainty (e.g. Villarini and Krajewski, 2010)
27 and require advanced post-processing algorithms. While employing weather radar observations it is crucial to perform an
28 advanced quality control (QC) of the data, which consists of clearing it from erroneous echoes (groundclutter, effects of
29 anomalous beam propagation, and biological scatterers such as birds and insects, etc.), correcting distorted data, and
30 quantitative estimation of the final data uncertainty. Detailed descriptions and reviews of currently used methods of QC of
31 radar data, which identify individual uncertainty components and address their combined effects, are commonly found in
32 literature (see e.g., Steiner and Smith, 2002; Berenguer et al., 2006; Cho et al., 2006; Gourley et al., 2007; Park et al., 2009;
33 Zhang et al., 2011; Krajewski et al., 2011; Szturc et al., 2012; Ośródkka et al., 2014). Many new dual-polarization-based
34 quality control algorithms are being implemented in radar signal processors and are part of their own software.

35 The quantity called quality index (*QI*) plays an increasingly important role in quality control of weather radar data
36 (e.g., Einfalt et al., 2010; Michelson et al., 2014), as it provides quantitative information on the quality of data, but can also
37 be used to generate more reliable individual products (Ośródkka and Szturc, 2015), to produce composite maps (Fornasiero et
38 al., 2006; Sandford and Gaussiat, 2012; Jurczyk et al., 2020a) or QPE based on multi-source information (Jatho et al., 2010;
39 Jurczyk et al., 2020b; Méri et al., 2021).



40 Huge effort to resolve quality-related issues in radar observations has been made by various international research
41 programmes, such as COST-717 (Michelson et al., 2005) and COST-731 (Rossa et al., 2010), EUMETNET OPERA
42 (Huuskonen et al., 2014; Saltikoff et al., 2019), the BALTRAD project (Michelson et al., 2018), and others.

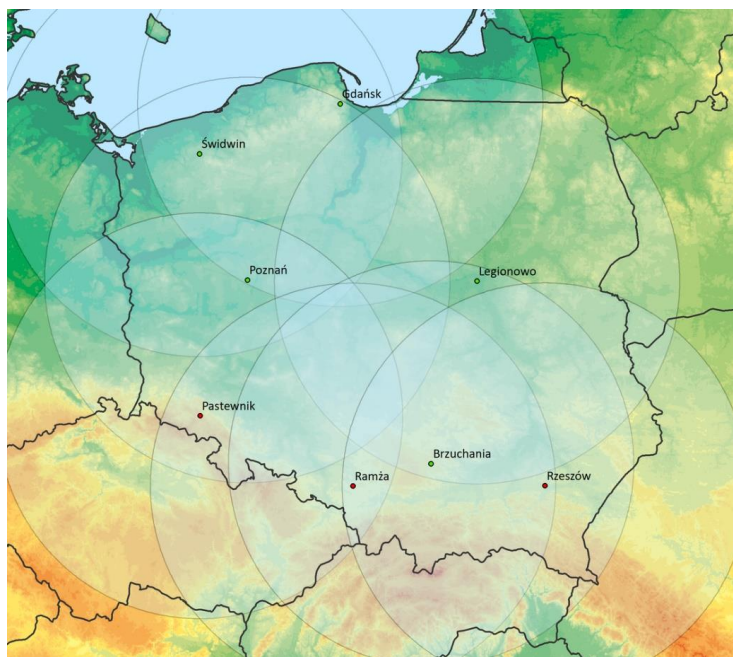
43 Different QC systems are designed to suit specific local conditions and are implemented in individual national
44 meteorological services, e.g. ROPO in Finland (Peura, 2002), NMQ in NOAA, USA (Zhang et al., 2012), RADVOL-QC in
45 Poland (Ośródka 2014), qRad in Slovakia (Méri et al., 2021).

46 In the Polish national meteorological and hydrological service, i.e. the Institute of Meteorology and Water
47 Management – National Research Institute, the RADVOL-QC system works operationally to perform QC of radar data
48 delivered by the Polish weather radar network POLRAD (Ośródka et al., 2014; Szturc et al., 2018). The main objective of
49 this study is to present new, more effective algorithms incorporated into the RADVOL-QC system which are able to
50 effectively deal with the abovementioned disturbances in radar data.

51 The paper is structured as follows: first, the RADVOL-QC system, its structure and applied approaches are briefly
52 presented (Section 2); then new solutions in the field of non-meteorological echo detection, incorporated into the RADVOL-
53 QC after the publication describing its earlier version, are discussed in Section 3, which is the essential part of the paper;
54 next, algorithms for correcting these detected distorted echoes are described (Section 4); finally, there is a brief description
55 of the verification of the system's effectiveness (Section 5), followed by a concise summary (Section 6).

56 2. Description of the RADVOL-QC system for the Polish weather radar network

57 2.1. Polish weather radar network POLRAD



58
59 **Figure 1: Coverage of the area of Poland by weather radar network POLRAD with 250-km range as of 2021.**

60 The algorithms for quality control of weather radar data described in the paper have been designed for Polish weather radar
61 network POLRAD, operated by the Institute of Meteorology and Water Management – National Research Institute (IMGW).
62 The network consists of eight C-band Doppler radars (Fig. 1) from which three are polarimetric. All the radars were
63 manufactured by European company Leonardo S.p.A., formerly Gematronik (Germany). The main parameters of the radars



64 and designed scan strategy are listed in Table 1. There is a plan in place to replace all radars in this network with dual-
 65 polarization ones and to expand it by two more radars in the years 2022-2023.

66

67 **Table 1. Parameters and scan strategy for radar reflectivity scans used in weather radars of the POLRAD network.**

Parameter	Value
Frequency (band)	5.5 GHz (C-band)
Beam polarization	Single (5) and dual (3)
Beam width	1°
Sampling along the radar beam	1 km
Number of azimuths	360
Maximum range	250 km
Number of elevations	10
Elevation angles	0.5, 1.4, 2.4, 3.4, 5.3, 7.7, 10.6, 14.1, 18.5, and 23.8°
Temporal resolution	10 min

68 **2.2. Structure of the RADVOL-QC system**

69 The 3-D raw data, so-called volumes, generated by POLRAD radars are quality controlled by the RADVOL-QC system. The
 70 RADVOL-QC quality control system includes data correction and determination of QI resulting from each recognized error
 71 source (Ośródko et al., 2014). The QC applies to each radar bin – a point in space that is assigned a single measurement. In
 72 the case of dual-polarization measurements, which offer more possibilities for efficient action but require different
 73 techniques (Bringi et al., 2011), the quality control algorithms constitute a separate category and their names are prefixed
 74 with “DP”. Quality control of Doppler data, i.e. velocities, also carried out in RADVOL QC is not described in this paper.

75 The different kinds of errors taken into consideration by the RADVOL-QC system can be divided into several groups.

76 *Errors connected with radar beam geometry* and effects related to increasing distance from the radar site along the
 77 beam, such as beam broadening, increasing distance between neighbouring bins and increasing height of the radar beam
 78 above ground level. As a result, extrapolation to the Earth’s surface is burdened with higher and higher errors along with
 79 distance from the radar site. Thus, to compensate rainfall underestimation due to these range-related problems, a correction is
 80 performed. It involves two factors: the altitude of the radar beam above ground level and a scaling function that modifies the
 81 correction magnitude depending on the precipitation type, i.e. limits its value for convective precipitation.

82 *Disturbance by non-meteorological echoes.* Such kinds of echoes are mainly caused by (i) groundclutter (mountains
 83 or high artificial structures located close to the radar site), (ii) external signals from RLAN emitters or the sun interfering
 84 with radar signals; these external signals are usually visible in the radar image as spikes pointing from the emitter towards
 85 the radar site, and can be removed using a geometrical algorithms that analyse the variability of the echo along and across
 86 the radar beam, (iii) small-scale measurement noise, so called speckles, and (iv) biological targets such as birds or insects.

87 *Other groups of errors* result from (i) beam blockage on terrain (mountains) causing a decrease in radar signal, which
 88 is corrected using a digital terrain map, (ii) attenuation in rain, especially if it is heavy, corrected by iterative estimation of
 89 signal loss along the beam path in cases of single-polarization radars and by an algorithm based on polarimetric information
 90 in cases of dual-polarization radars, and (iii) anomalous propagation of the radar beam which causes, for example, echoes
 91 received from non-meteorological (terrain) and meteorological (hydrometeors) objects located outside the radar range.

92 Each category of errors burdening radar data is characterized by specific properties, especially spatial and temporal
 93 structure. As a result, different approaches for their diagnosis and correction are required (Table 2).

94

95 **Table 2. List of quality control algorithms employed in the RADVOL-QC system for radar reflectivity data measured by single-
 96 and dual-polarization (dual-pol) weather radars in order of the data processing chain.**

Algorithm	Task	Correction technique
-----------	------	----------------------



BROAD	Quality characterisation due to broadening of the radar beam	Analysis of geometry of the radar beam cross-section
DP.TURBINE	Detection of non-meteorological echoes, especially from wind farms, for dual-pol radars	Fuzzy logic algorithm based on dual-pol parameters: Z_{DR} , ρ_{HV} , $sd(Z)$, $sd(Z_{DR})$, $sd(\Phi_{DP})$
DP.NMET	Detection of non-meteorological echoes: biological, anomalous propagation, etc., for dual-pol radars	Decision tree based on dual-pol parameters: ρ_{HV} , $sd(\Phi_{DP})$, and $sd(Z_{DR})$
TURBINE	Detection of non-meteorological echoes, especially from wind farms and other obstacles	Long-term analysis of radar echoes at the lowest elevation (static masks)
SPIKE	Detection of non-meteorological echoes of spike type because of RLAN interference	Analysis of variability of radar echoes across and along the radar beam
INTERP	Corrections: interpolation of non-meteorological echoes detected by the algorithms: DP.TURBINE, DP.NMET, TURBINE, and SPIKE	Values from a neighbouring higher elevation after adjustment to the vicinity mean (for DP.TURBINE, DP.NMET, and TURBINE). Interpolation from not burdened neighbouring bins across the radar beam (for SPIKE)
NMET	Removal of non-meteorological echoes: biological, caused by anomalous propagation, etc.	Analysis of altitude and intensity of echoes
SPECK	Removal of measurement noise (speckles)	Analysis of a given bin vicinity and analysis of a spatial distribution of echo intensity
MHV	Compensation of underestimation due to distance to the Earth's surface	Corrections due to extrapolation down to the Earth's surface
BLOCK	Correction of the partial and total radar beam blockage by terrain, buildings, etc.; detection of groundclutter	Analysis of the geometry of the radar beam and digital terrain map
DP.ATT	Correction of the radar beam attenuation in precipitation for dual-pol radars	Analysis of dual-pol parameters
ATT	Correction of the radar beam attenuation in precipitation for single-pol radars (only one of these two: DP.ATT and ATT can be used for a given radar)	Analysis of attenuation along the path of the radar beam (based on specific attenuation)

97

98 Individual quality indices (QI_i) are determined in the frame of each i -th RADVOL-QC algorithm separately and after
 99 the whole quality control chain the final total quality index QI is determined using multiplicative formula (Einfalt et al.,
 100 2010; Ośródko et al., 2014). Its values range from 0 for extremely bad to 1 for perfect quality data.

101 In this paper only the new and enhanced algorithms implemented into the RADVOL-QC system after publication of
 102 the earlier paper by Ośródko et al. (2014) are described in detail. Since this time the system has continued to be developed,
 103 including within the European BALTRAD project (Michelson et al., 2018) and as part of IMGW's statutory duties.

104 3. New solutions for the detection of non-meteorological echoes

105 3.1. New challenges

106 The recent dramatic increase in the number of RLAN signals interfering with radar echoes (e.g., Saltikoff, 2016) as well as
 107 the greater number of wind farms used for energy generation (e.g., Hood et al., 2010) has created new and serious challenges
 108 to the developed QC algorithms, despite the fact that the commonly used approaches show good performance in many
 109 observed cases.

110 The first problem, that of radio interference, is becoming more and more difficult to handle because of a growing
 111 number of such echoes. A team of experts from around the world representing institutions involved in weather radar
 112 measurements, including the EUMETNET OPERA programme, issued the following drastic statement: "As an extreme
 113 solution, and on a theoretical basis, an entire C-band network could be replaced by a dense network of X-band radars (...)"
 114 (Saltikoff et al., 2016). Nonetheless, the interference must be removed from radar-based precipitation data before ingestion
 115 into any application, such as input into hydrological rainfall-runoff modelling or assimilation into mesoscale numerical
 116 weather prediction models. A significant problem with the RLAN-derived echoes, so called spikes, is that although they may
 117 be partially removed or decreased due to the low threshold of signal quality index (SQI) of radar data, this in fact
 118 complicates their removal because it disrupts their spatio-temporal pattern applied in the relevant algorithm.

119 As a response to the increasing demand for renewable energy, the number of wind turbines is growing rapidly in
 120 many countries around the world. Their impact on weather radar performance has been extensively studied in recent years,

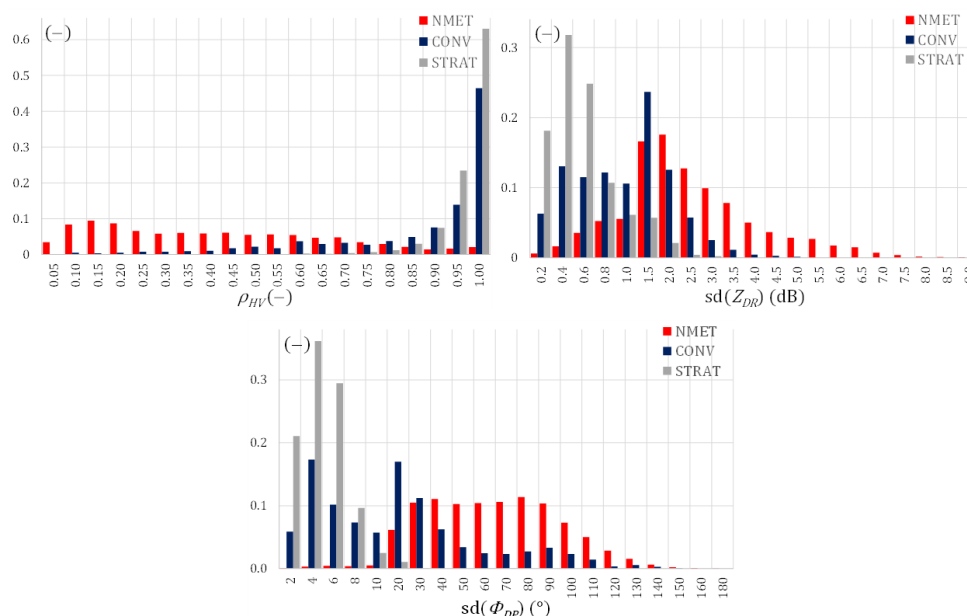


121 with several cases of wind turbine clutter observed in meteorological radar applications (Isom et al., 2009; Norin and Haase,
 122 2012; Angulo et al., 2015; Norin, 2015). The main objective of these studies was to characterize and try to mitigate wind
 123 turbine clutter, mainly by means of digital signal processing such as clutter-filtering techniques. However, the Doppler
 124 information that is often used for the removal of stationary target returns is not likely to be appropriate in this case because
 125 wind turbine blades are constantly rotating and, consequently, provide a non-zero Doppler signature (e.g., Angulo et al.,
 126 2015).

127 Erroneously estimated rainfall amounts propagate through hydrological models, affecting hydrologic simulations and
 128 predictions. To mitigate or eliminate the aforementioned RLAN interference and effects of wind turbines in quantitative
 129 rainfall estimation and subsequent applications, this paper proposes the incorporation of enhanced automated approaches
 130 into the RADVOL-QC system.

131 3.2. Fuzzy logic scheme for polarimetric parameters – DP.TURBINE algorithm

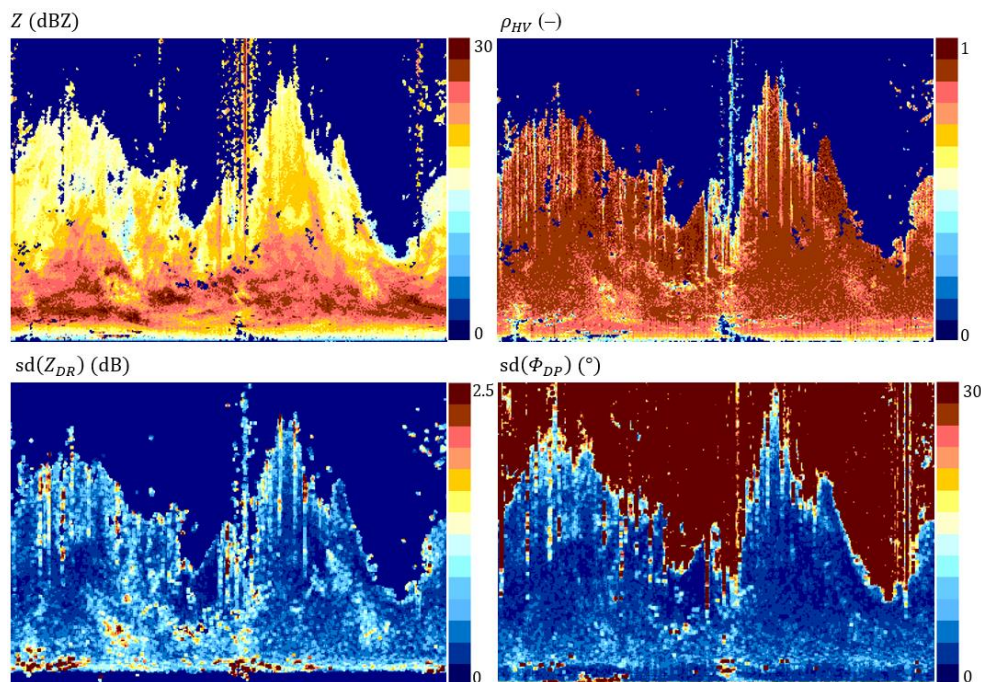
132 The algorithm named DP.TURBINE is used mainly for the detection of radar echoes generated by wind turbines; it employs
 133 a fuzzy logic scheme for selected polarimetric parameters (the definition of dual-polarimetric parameters can be found e.g.
 134 in Bringi and Chandrasekar, 2001). Preliminary analysis has been conducted to check which polarimetric parameters are
 135 most sensitive to non-meteorological echoes. This was investigated by means of histograms for the following classes of radar
 136 echoes: non-meteorological and meteorological, where the latter is divided into two types: convective and stratiform
 137 precipitation. Three parameters were finally selected to be employed in this algorithm: the differential reflectivity factor
 138 Z_{DR} (dB), the cross-correlation coefficient between horizontally and vertically polarized radar returns ρ_{HV} , and the
 139 differential phase Φ_{DP} (°). The ρ_{HV} is employed in the algorithm directly, whereas for the others standard deviations $sd(Z_{DR})$
 140 and $sd(\Phi_{DP})$ computed within grids of 3 bins x 3 bins are employed. Histograms of the selected parameters obtained for
 141 Ramža radar from two days – one with a convective event and the second with a stratiform one – are presented in Fig. 2.
 142



143
 144 **Figure 2:** Histograms for selected polarimetric parameters from the top-left: ρ_{HV} , $sd(Z_{DR})$, and $sd(\Phi_{DP})$, for three classes of radar
 145 echoes: non-meteorological (NMET, in red), meteorological convective (CONV, in navy), and meteorological stratiform (STRAT,
 146 in grey). Ramža radar, data from two days: 1 September 2018 and 21 February 2019, the lowest elevation.



147 It is notable that for correlation coefficient ρ_{HV} , the non-meteorological echoes generate values clearly different to
148 those for meteorological echoes, and the range of overlap is quite narrow. The standard deviations $sd(Z_{DR})$ and $sd(\Phi_{DP})$
149 also differ in values for the three classes, especially for stratiform precipitation. The above information collected for these
150 three parameters allows one to deduce the presence of non-meteorological echoes with a relatively high certainty.
151



152 **Figure 3:** Radar measurement fields from the top-left: Z , ρ_{HV} , $sd(Z_{DR})$, and $sd(\Phi_{DP})$. Ramza radar, the lowest elevation, 21
153 February 2019, 16:40 UTC. At the bottom: definition of axes in polar coordinates.
154

155 In Fig. 3 examples of radar reflectivity Z along with the three polarimetric parameters investigated in the
156 DP.TURBINE algorithm are presented. All the radar pictures shown in this article, with the exception of those shown in Fig.
157 12, are presented in the polar coordinates: the horizontal axis gives the azimuth (α) in degrees, and the vertical axis gives the
158 distance from the radar site (l) in km.

159 The evident non-meteorological spike echoes are especially visible on ρ_{HV} data, whereas non-meteorological from
160 terrain and other obstacles are mainly visible on $sd(Z_{DR})$ data.

161 Having selected the most appropriate polarimetric parameters, a fuzzy logic approach was applied to categorize radar
162 bins into meteorological and non-meteorological echoes. Calibration of the scheme consists in the determination of the
163 function parameters for each class of echoes: meteorological and non-meteorological, including those from wind farms (Fig.
164 4).

165

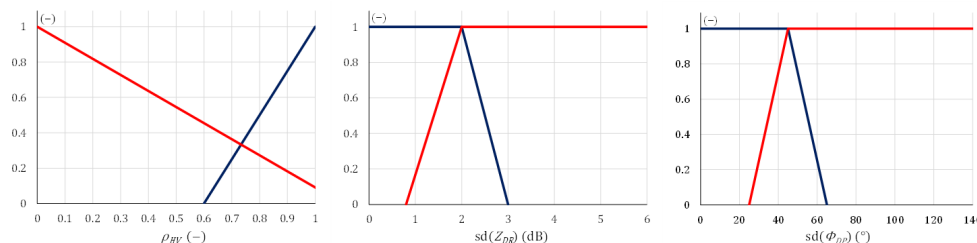


Figure 4: Membership functions for selected polarimetric parameters from the left: ρ_{HV} , $sd(Z_{DR})$, and $sd(\Phi_{DP})$ determined for meteorological (in navy) and non-meteorological echoes (in red).

166
 167
 168

169 For both echo classes, values of relevant membership functions for all three selected parameters are aggregated as
 170 weighted sums:

$$171 \mu(class) = \sum_{i=1}^3 \mu_i(class) \cdot W_i(class) \quad (1)$$

172 where *class* is the echo class (meteorological or non-meteorological), *i* is the parameter number, 3 is the number of
 173 parameters, $\mu_i(class)$ is the membership function for *i*-th parameter for echo class *class*, and $W_i(class)$ is the weight of *i*-
 174 th parameter for echo class *class*. These weights equal 1.0, 0.5, and 1.0 for parameters ρ_{HV} , $sd(Z_{DR})$, and $sd(\Phi_{DP})$,
 175 respectively. Comparison of the weighted sums decides which echo class a considered radar bin belongs to.

176 The designed algorithm proved to be effective, especially for the detection of wind turbines. The effectiveness of the
 177 algorithm was checked on data in the form of monthly precipitation accumulation determined for the lowest antenna
 178 elevation (0.5°), because at a higher elevation the number of this kind of non-meteorological echo is not significant. The
 179 radar reflectivity was transformed into precipitation using the Marshall-Palmer formula. The following categories of objects
 180 were identified based on a map of aeronautical obstacles of Poland provided by the Polish Civil Aviation Authority
 181 (<http://caa-pl.maps.arcgis.com/apps/webappviewer/index.html?id=252d2be2e6104adcb9be8201660a05b3/>): (i) wind
 182 turbines and wind farms, (ii) other disturbing objects, and (iii) undisturbed locations. Effectiveness (*effectiveness*) of the
 183 DP.TURBINE algorithm has been assessed by the formula:

$$184 effectiveness = 1 - \frac{R_{DP.TURBINE} - R_{bg}}{R_{raw} - R_{bg}} \quad (2)$$

185 where R_{raw} is the monthly uncorrected precipitation accumulation at the location of a given object; $R_{DP.TURBINE}$ is the
 186 precipitation accumulation in the same place after using the DP.TURBINE algorithm for the detection of obstacles and then
 187 the INTERP algorithm (see Section 4) for their correction; R_{bg} is the monthly precipitation accumulation determined for the
 188 undisturbed neighbourhood of a considered object.

189

190 Table 3. Monthly precipitation accumulations determined for the lowest elevation (0.5°) at locations of wind turbines, other
 191 disturbing objects, and undisturbed locations. Data from Ramża radar, September 2018.

Kind of object	Azimuth ($^\circ$)	Dist. from the radar site (km)	R_{raw} (mm) – raw data	$R_{DP.TURBINE}$ (mm) – after DP.TURBINE	R_{bg} (mm) – background	<i>effectiveness</i> of the algorithm
Wind turbines	16	54	1371	302	90	0.83
	331	38	1060	214	110	0.89
	270	68	1096	345	180	0.82
	253	41	745	189	150	0.93
	237	41	1359	264	140	0.90
	251	56	842	329	210	0.81
	233	91	784	401	280	0.76
	229	88	1302	708	270	0.58
Other disturbing objects	20	56	1161	272	90	0.83
	319	43	1486	279	135	0.89
	313	51	1874	166	100	0.96



	246	95	3543	1293	220	0.68
Undisturbed locations	100	79	189	187	187	1.00
	280	79	170	170	170	1.00
	10	119	149	137	137	1.00
	55	39	165	152	152	1.00

192

193

194

195

196

197

198

199

200

201

202

203

204

205

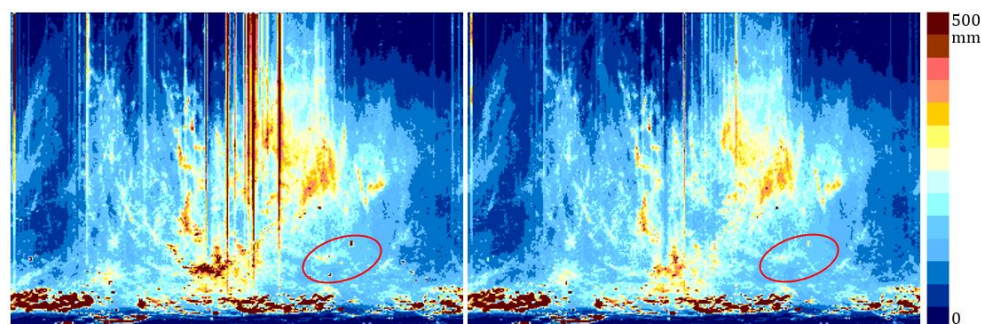
206

207

Table 3 shows the influence of the DP.TURBINE algorithm on the values of monthly accumulation of radar echoes in places where wind turbines and other obstacles (masts, chimneys) disturb the radar observations from Ramža radar. There are many such objects here and their monthly precipitation accumulations resulting from disturbance from these turbines often significantly exceed a thousand mm. The *effectiveness* of the developed algorithm for echoes from wind turbines in range of the Ramža radar, presented in Table 3, is on average 0.82. However, if the intensities of echoes from wind turbines are lower, this efficiency is lower.

In Fig. 5 an example of the DP.TURBINE running is also presented for the Ramža radar. Within this radar range a lot of obstacles can be visible in the monthly accumulations, but only a small number of them are due to wind turbines. The extremely dense strong echoes placed within a distance approximately 30 km from the radar site are a result of the industrial and urbanized area (the Upper Silesia conurbation) located close to the Ramža radar. The existence of high buildings produces such strong echoes due to side lobes from the radar beam. Other disturbances are caused by RLAN interference.

The efficiency of the DP.TURBINE algorithm is significantly visible in the right picture. It should be noted that the SPIKE algorithm for RLAN echo removal was also employed here. Example locations of wind turbines visible in the raw radar image are marked with a red ellipse.



208

209

210

211

Figure 5: Example of the performance of the DP.TURBINE algorithm from the left: raw data and data after detection of non-meteorological echoes by means of DP.TURBINE and SPIKE, and their interpolation with INTERP. Ramža radar, monthly accumulation of precipitation, the lowest elevation, September 2018. The red ellipse shows examples of echoes from wind turbines.

212

213

The individual quality index $QI_{DP.TURBINE}$ depends on the presence of a detected non-meteorological echo in a given bin according to equation:

214

$$QI_{DP.TURBINE} = \begin{cases} 0.75 & \text{bin with non-meteorological echo} \\ 1 & \text{bin without non-meteorological echo} \end{cases} \quad (3)$$

215

3.3. Decision tree for polarimetric parameters – DP.NMET algorithm

216

217

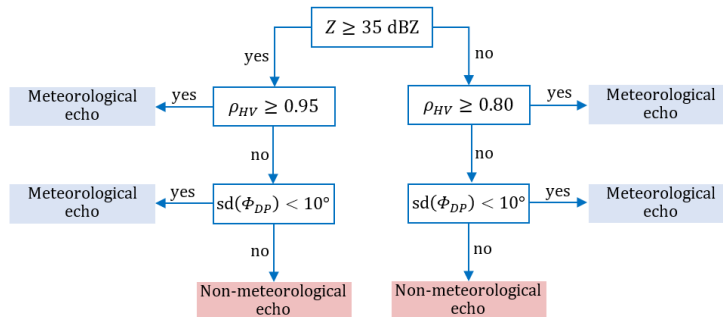
218

219

220

221

As opposed to the DP.TURBINE algorithm, which has been designed especially for wind turbine echoes, the DP.NMET is dedicated to different types of disturbances in weather radar measurements, caused not only by wind turbines but also by RLAN interference, anomalous propagation, biological objects, etc. The main idea proposed by Seo et al. (2015) is to use a decision tree, in which the following polarimetric parameters are employed: Z , ρ_{HV} , $sd(\Phi_{DP})$, and $sd(Z_{DR})$. The adaptation of this original scheme came down to tailoring parameters to local conditions and excluding the $sd(Z_{DR})$ parameter (Fig. 6).



222

223 **Figure 6: Flowchart describing the DP.NMET algorithm designed to detect non-meteorological echoes of different types for dual-**
 224 **polarization radars (based on the scheme from Seo et al., 2015).**

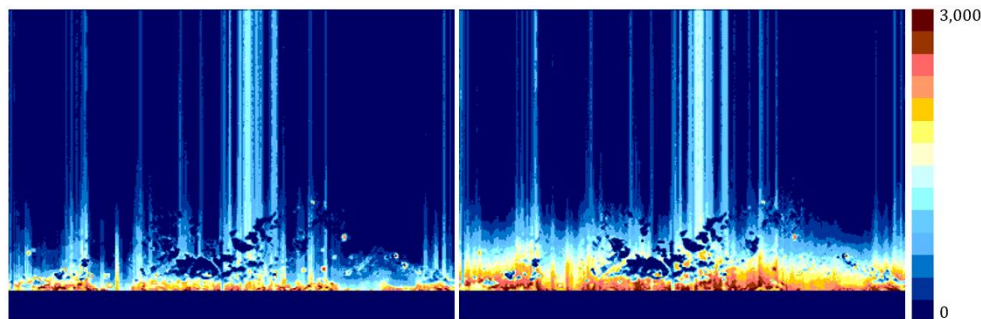
225 This flowchart can be written as one condition:

226 If $\{[(Z \geq (Z)_{thr}) \text{ and } (\rho_{HV} < (\rho_{HV})_{thr1})] \text{ or } [(Z < (Z)_{thr}) \text{ and } (\rho_{HV} < (\rho_{HV})_{thr2})]\}$ and $[sd(\Phi_{DP}) \geq$
 227 $sd(\Phi_{DP})_{thr}]$ then a given echo is non-meteorological (4)

228 where values of the thresholds have been estimated for the radars of the POLRAD network as follows: $(Z)_{thr} = 35$ dBZ,
 229 $(\rho_{HV})_{thr1} = 0.95$, $(\rho_{HV})_{thr2} = 0.80$, and $sd(\Phi_{DP})_{thr} = 10^\circ$.

230 The main approach of the algorithm is that the basic polarimetric parameter for differentiation between
 231 meteorological and non-meteorological echoes is the correlation coefficient ρ_{HV} : the echo is non-meteorological if the value
 232 is lower than a defined threshold, however for lower reflectivity the threshold is decreased, i.e. fewer echoes are classified as
 233 non-meteorological. Because the ρ_{HV} has a wide overlapping range for the meteorological and non-meteorological classes
 234 (see Sect. 3.2), additional verification is needed since false detection of non-meteorological echoes occurs too often. For this
 235 reason, in the next step the standard deviation $sd(\Phi_{DP})$ is used to confirm the preliminary classification: if the value is higher
 236 than a defined threshold, the echo is recognized as non-meteorological.

237



238

239 **Figure 7: Numbers of non-meteorological echoes detected separately by algorithms from the left: DP.TURBINE and DP.NMET.**
 240 **Ramža radar, September 2018, the lowest elevation. Up to 25 km from the radar, the algorithm is not applied.**

241 Fig. 7 shows how many times the DP.TURBINE (discussed in Sect. 3.2) and DP.NMET algorithms separately
 242 detected non-meteorological echoes during one month for Ramža radar data at the lowest elevation. The total number was 3
 243 thousand out of approximately 4,320 measurements.

244 Both algorithms are not applied up to 25 km from the radar site because within the RADVOL-QC system one of the
 245 SPECK sub-algorithms (see Ošródká et al., 2014) operates in this area, replacing the data on the lowest elevation with data
 246 from the adjacent higher one, which explains the wide strip near the radar site where no echoes were detected.

247 It turned out that the DP.TURBINE algorithm is better at extracting small-area echoes associated with wind turbines,
 248 while the DP.NMET algorithm detects more other non-meteorological echoes, especially those located near the radar (but



249 outside the aforementioned 25-km strip) caused by side lobes of the radar beam hitting various types of obstacles. It is
250 noticeable that both algorithms are also sensitive to other types of non-meteorological echoes, especially those connected to
251 RLAN interference of spike type. As mentioned in Section 3.2, the Ramża radar generates the most disturbed data, especially
252 in the vicinity of the radar, due to its location near a large industrial and urban area.

253 Similarly to the previous algorithm, the individual quality index $QI_{DP.NMET}$ depends on the presence of a detected
254 non-meteorological echo in a given bin:

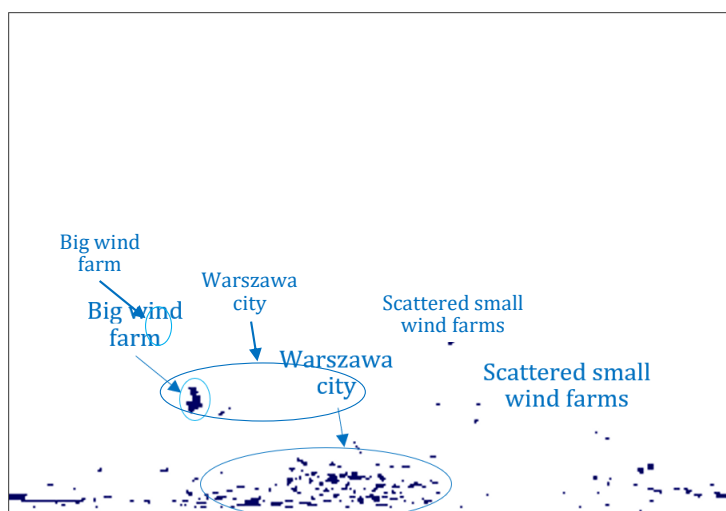
$$255 \quad QI_{DP.NMET} = \begin{cases} 0.75 & \text{bin with non-meteorological echo} \\ 1 & \text{bin without non-meteorological echo} \end{cases} \quad (5)$$

256 3.4. Static maps (masks) of echoes – TURBINE algorithm

257 The algorithm using static maps (masks) of groundclutter of various origins is a very simple but effective tool. However, it
258 requires relatively frequent updating of maps depending on the intensity of obstacle changes in the range of a given radar.
259 Fig. 8 shows an example of such a mask for the Legionowo radar located in central Poland. It is near Warszawa (Warsaw)
260 city, which causes a significant number of obstacles to the south of the radar site. Moreover, echoes from various kinds of
261 wind turbines are visible here.

262 The following algorithm has been developed for the semi-automatic generation of static echo maps from wind
263 turbines and other groundclutter. At the first stage, fields of precipitation are generated for non-rainy time-steps (when a
264 number of rainy bins is below a defined threshold) for the lowest elevations of each radar. Every few months they are
265 accumulated, and on this basis maps of permanent echoes from wind farms as well as residential and industrial buildings are
266 generated for bins exceeding a certain threshold value, specific for each radar. At the last stage, the maps are manually
267 corrected by comparing them with the initial fields and with previous masks in order to exclude from the masks echoes such
268 as those from the mountains to avoid significant reduction of precipitation in these areas.

269



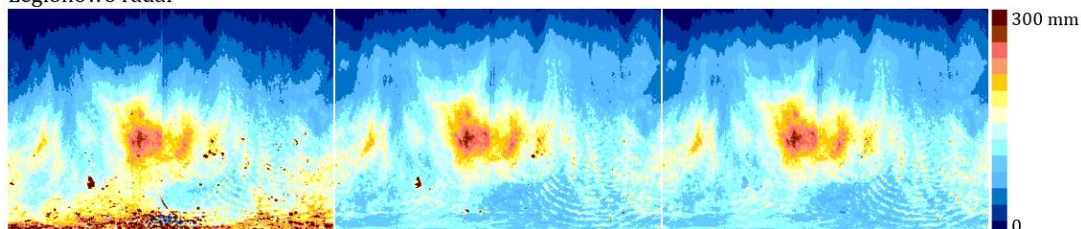
270
271 **Figure 8: Example of a mask of non-meteorological permanent echoes. Legionowo radar, the lowest elevation.**

272 Figure 9 shows the monthly precipitation sums for selected radars of the POLRAD network: from raw data and after
273 processing with the RADVOL-QC system without and with the TURBINE algorithm; the latter stands for the complete
274 system. The RADVOL-QC system proved to be very effective even without the use of the TURBINE algorithm because
275 some other algorithms, especially those based on data from dual polarization radars, detect echoes from wind turbines as
276 well. This improvement is especially noticeable for radars covering mountainous areas, such as Pastewnik and Ramża, as

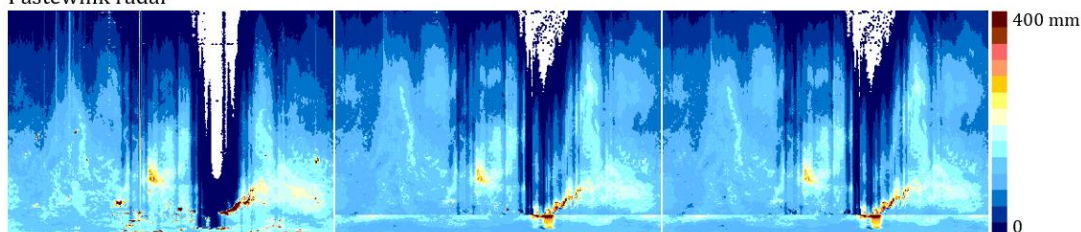


277 well as highly urbanized areas such as Legionowo and Ramża. More effective removal of wind farms employing the
 278 TURBINE algorithm for Legionowo can be explained by the fact that this radar is not dual-polarimetric.
 279

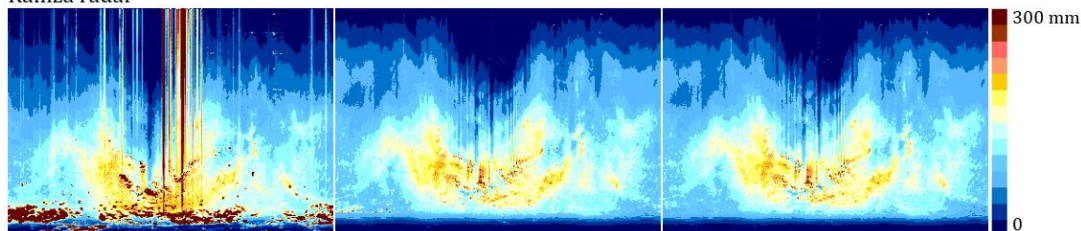
Legionowo radar



Pastewnik radar



Ramża radar



280 Figure 9: Comparison of the monthly sums of radar precipitation from (from the left): raw data, data after processing by the
 281 RADVOL-QC system without the TURBINE algorithm, and with the TURBINE algorithm (i.e. the complete RADVOL-QC
 282 system). Legionowo, Pastewnik, and Ramża radars, the lowest elevations. October 2019.
 283

284

285 The individual quality index $Q_{TURBINE}$ is lowered in the bins located within the mask of permanent non-
 286 meteorological echoes:

$$287 \quad Q_{TURBINE} = \begin{cases} 0.75 & \text{bin with non-meteorological echo} \\ 1 & \text{bin without non-meteorological echo} \end{cases} \quad (6)$$

288 3.5. Geometrical algorithms for the removal of RLAN interference – SPIKE algorithm

289 The Polish radar network POLRAD consists of eight radars, but only three of them are equipped with the functionality of
 290 dual-polarisation of the radar beam. Therefore, algorithms that do not use polarimetric parameters to remove non-
 291 meteorological echoes are still very important to ensure the appropriate quality of data, especially as not all measurement
 292 disturbances can be removed through applying polarimetric data.

293 In C-band weather radars, signals generated by external RLAN systems, and also from the sun – so-called spike
 294 echoes – are interpreted by radar as precipitation echoes. The shape of these echoes is very specific: in Cartesian radar
 295 images they have the form of elongated narrow spike-shaped echoes, located along the radar beam, sometimes with high
 296 reflectivity.

297 The SPIKE algorithm actually consists of a set of sub-algorithms that are sensitive to the various properties of this
 298 type of radar echo. Since this algorithm has been an important element of the RADVOL-QC system from the very



299 beginning, it has been described in detail in the earlier work of Ośródko et al. (2014). However, it has undergone major
300 changes since then, so in this paper the areas where the most significant changes took place will be described in greater
301 detail.

302 In the algorithm for eliminating this type of echo from radar pictures, the spatial structure of the reflectivity field is
303 analysed separately for each elevation. The algorithm is divided into several sub-algorithms used to remove different types
304 of spike echoes, which are named in simple terms:

- 305 – “wide”,
- 306 – “narrow”,
- 307 – “discontinuous”,
- 308 – “shorter longitudinal”,
- 309 – “inverse”.

310

311 *Sub-algorithm for “wide” spike detection*

312 This sub-algorithm is used for spikes if the echo percentage coverage of a given elevation does not exceed a pre-set threshold
313 value. The echo changeability is examined by means of its local variance across and along the radar beam: echoes are
314 classified as “potential” spikes when the variance of reflectivity across the beam is high and low along the beam. This
315 algorithm was described in an earlier paper by Ośródko et al. (2014).

316

317 *Sub-algorithm for “narrow” spike detection*

318 The next algorithm is used to detect spike echoes of small width, i.e. not wider than 5°. In the first step, for a given radar bin
319 in which a radar echo is observed, the reflectivity values in the bins located at the angular distance from a given azimuth and
320 at the same distance from the radar site are examined if they are sufficiently weak – in this case a potential spike echo is
321 recognized in this bin. This check is repeated for all possible shorter angular distances as well. This algorithm was also
322 described by Ośródko et al. (2014).

323

324 *Sub-algorithm for “discontinuous” spike detection*

325 This newly introduced sub-algorithm is applied to spike echoes of generally elongated shape, but discontinuous along and
326 across the radar beam. The sub-algorithms described above cannot manage with such spikes due to discontinuities in their
327 pattern.

328 The algorithm consists of two steps: at first potential azimuths with “discontinuous” spikes are detected, then they are
329 confirmed by appropriate changeability of the radar beam. For the lowest elevation the first step is omitted because this scan
330 can be very rainy, so detection of potential spikes may not be efficient and the azimuths with potential spikes are taken from
331 the neighbouring higher elevation.

332 In the below procedure for each azimuth α for a given elevation ε (apart from the lowest one) the echo bins are
333 counted along the whole radar beam to obtain the $n(\varepsilon, \alpha)$ values:

$$334 \quad n(\varepsilon, \alpha) = \sum_{l=1}^N i(\varepsilon, \alpha, l), \quad \text{where: } i(\varepsilon, \alpha, l) = \begin{cases} 1 & Z(\varepsilon, \alpha, l) = \text{echo} \\ 0 & Z(\varepsilon, \alpha, l) = \text{noecho} \end{cases} \quad (7)$$

335 where N is the number of samplings along the radar beam.

336 The $p(\varepsilon, \alpha)$ value is determined as the larger of the modulus values of differences between $n(\varepsilon, \alpha)$ and the values in
337 the adjacent azimuths $\alpha - 1$ and $\alpha + 1$:

$$338 \quad p(\varepsilon, \alpha) = \max(|n(\varepsilon, \alpha - 1) - n(\varepsilon, \alpha)|, |n(\varepsilon, \alpha + 1) - n(\varepsilon, \alpha)|) \quad (8)$$



339 Then for the analysed beam α the two means are calculated: $\overline{p_1(\varepsilon, \alpha)}$ and $\overline{p_2(\varepsilon, \alpha)}$ within the ranges $\pm p_1^{thr}$ and
340 $\pm p_2^{thr}$ respectively, and the value $P(\varepsilon, \alpha)$ is determined:

$$341 \quad P(\varepsilon, \alpha) = \overline{p_1(\varepsilon, \alpha)} - \overline{p_2(\varepsilon, \alpha)} \quad (9)$$

342 Potential “discontinuous” spikes are found in the radar beams on azimuths that meet the following condition:

$$343 \quad \text{If } (P(\varepsilon, \alpha) > P_{thr1}) \text{ or } [(P(\varepsilon, \alpha) > P_{thr2}) \text{ and } (p(\varepsilon, \alpha) > P_{thr3})] \text{ then there is a potential spike in the azimuth } \alpha \quad (10)$$

344 where P_{thr1} , P_{thr2} , and P_{thr3} are the threshold values.

345 Due to the specific shape of this type of echo, an additional check is introduced in order to smooth the field of
346 relevant potential spikes: azimuth α is considered a potential spike if azimuths $\alpha - 1$ and $\alpha + 1$ are potential ones.

347 In the final step, bins in azimuths with such potential spike echoes are confirmed for each elevation employing
348 variances calculated across the radar beam $\text{var}_{across}(\varepsilon, \alpha, l)$, also taking into account the “no echo” values:

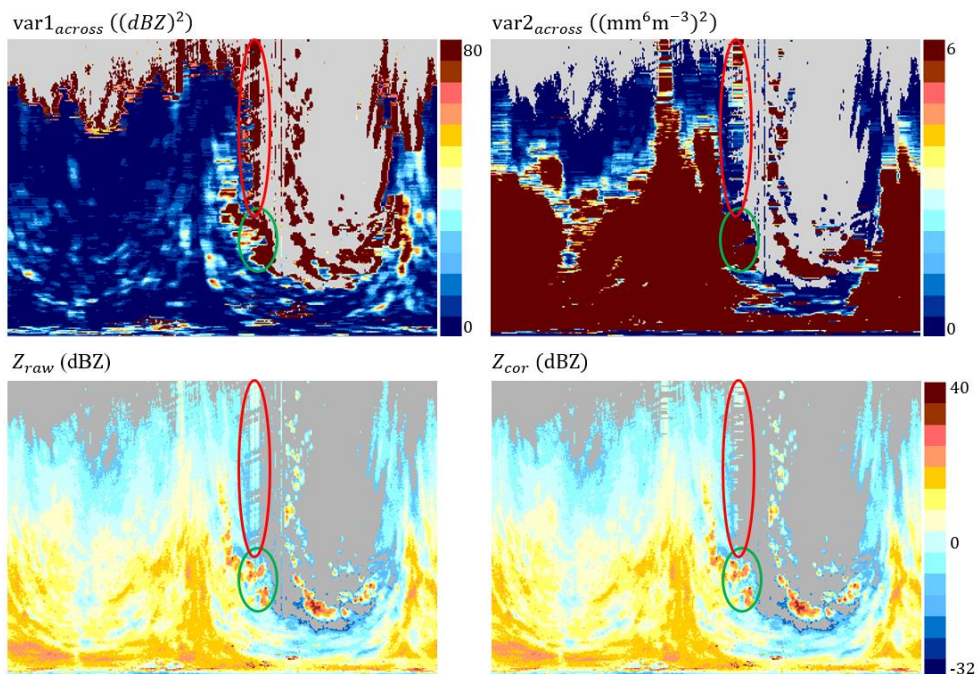
$$349 \quad \text{If } [(\text{var1}_{across}(\varepsilon, \alpha, l) > \text{var}_{thr1}) \text{ and } (\text{var2}_{across}(\varepsilon, \alpha, l) < \\ 350 \quad \text{var}_{thr2})] \text{ then there is a potential spike in the radar bin } (\varepsilon, \alpha, l) \quad (11)$$

351 where the variance $\text{var1}_{across}(\varepsilon, \alpha, l)$ is calculated for reflectivity in dBZ and $\text{var2}_{across}(\varepsilon, \alpha, l)$ for reflectivity in
352 $\text{mm}^6 \text{m}^{-3}$, and var_{thr1} and var_{thr2} are the threshold values.

353 The concept of the above formula is that “discontinuous” spike echoes have a specific variance of radar reflectivity in
354 echoes across the radar beam. The variance calculated in dBZ, hence logarithmic ($1 \text{ dBZ} = 10 \cdot \log_{10}(1 \text{ mm}^6 \text{ m}^{-3})$), is high
355 for echoes of this type (Fig. 10, on the left). However, high variance in dBZ is also characteristic of intense meteorological
356 echoes, especially those originating from convective rainfall. On the other hand, in the case of non-logarithmic values (mm^6
357 m^{-3}), the variance of meteorological echoes is relatively high, because their values are generally higher and at the same time
358 more internally differentiated than that of spike echoes. Thus, the algorithm for the detection of “discontinuous” spike
359 echoes assumes that they are both characterized by a high variance calculated for reflectivity in dBZ and a relatively low
360 variance calculated for reflectivity in $\text{mm}^6 \text{m}^{-3}$.

361 The example in Fig. 10, shows that the criterion associated with high dBZ values clearly indicates radial echoes
362 located south and slightly west as “discontinuous” spikes, but also at the edges of clearly meteorological echoes. On the
363 other hand, the criterion based on the values of $\text{mm}^6 \text{m}^{-3}$ prevents meteorological echoes from classification as potential
364 spike echoes, which could occur in the case of a few small echoes marked by a green ellipse. The red ellipse shows example
365 of spike echoes. The echoes at the edges of meteorological echoes, which were classified as “potentially” non-
366 meteorological by both conditions, were finally not confirmed as spikes (see paragraph “Verification of potential spike-type
367 echoes”).

368



369
 370 **Figure 10: Example of the performance of the SPIKE and INTERP algorithms. At the top: variances of radar reflectivity across**
 371 **the radar beam calculated from the left, in dBZ and mm⁶ m⁻³. At the bottom: radar reflectivity from the left, raw dBZ (Z_{raw})**
 372 **and corrected (interpolated) (Z_{cor}). In the red ellipse: “discontinuous” spike echoes; in the green ellipse: meteorological echoes**
 373 **correctly not qualified as spikes. Świdwin radar, the lowest elevation, 9 May 2019, 11:00 UTC.**

374 *Sub-algorithm for “shorter longitudinal” spike detection*

375 This also newly introduced sub-algorithm is relatively aggressive, so it is only used for the radars which are extremely
 376 burdened with spike echoes, just for the lowest elevation.

377 For the lowest elevation, using the appropriate threshold for reflectivity (Z_{thr}), for each radar bin (ϵ, α, l) the
 378 numbers of successively adjacent bins of reflectivity above the threshold, along $size_{along}(\epsilon, \alpha, l)$ and across
 379 $size_{across}(\epsilon, \alpha, l)$ the given radar beam, are counted. The “shorter longitudinal” spike echo in a bin (ϵ, α, l) is detected if the
 380 following condition is met:

$$381 \text{ If } (size_{along}(\epsilon, \alpha, l) > (size_{along})_{thr}) \text{ and } (size_{across}(\epsilon, \alpha, l) <$$

$$382 (size_{across})_{thr}) \text{ then there is a “shorter longitudinal” spike in the radar bin } (\epsilon, \alpha, l) \quad (12)$$

383 where $(size_{along})_{thr}$ and $(size_{across})_{thr}$ are the threshold values.

384

385 *Sub-algorithm for “inverse” spike detection*

386 The term “inverse” spike-type echo means an area in this case of decreased reflectivity values in the shape of a spike aimed
 387 at the radar site visible on a radar picture. Such echoes are most often the result of beam blocking, but the BLOCK algorithm
 388 does not detect them by means of a digital terrain map.

389 This sub-algorithm is used only for the two lowest elevations. For each azimuth the radar bins with potential
 390 “inverse” spike echoes are found using the following condition:

$$391 \text{ If } ((Z(\epsilon, \alpha - d, l) - Z(\epsilon, \alpha, l)) > Z_{thr}) \text{ and } ((Z(\epsilon, \alpha + d, l) - Z(\epsilon, \alpha, l)) >$$

$$392 Z_{thr}) \text{ then there is a potential spike in the radar bin} \quad (13)$$



393 where Z_{thr} is the threshold value. This procedure is performed for values of d from 1 to d_{thr} .

394

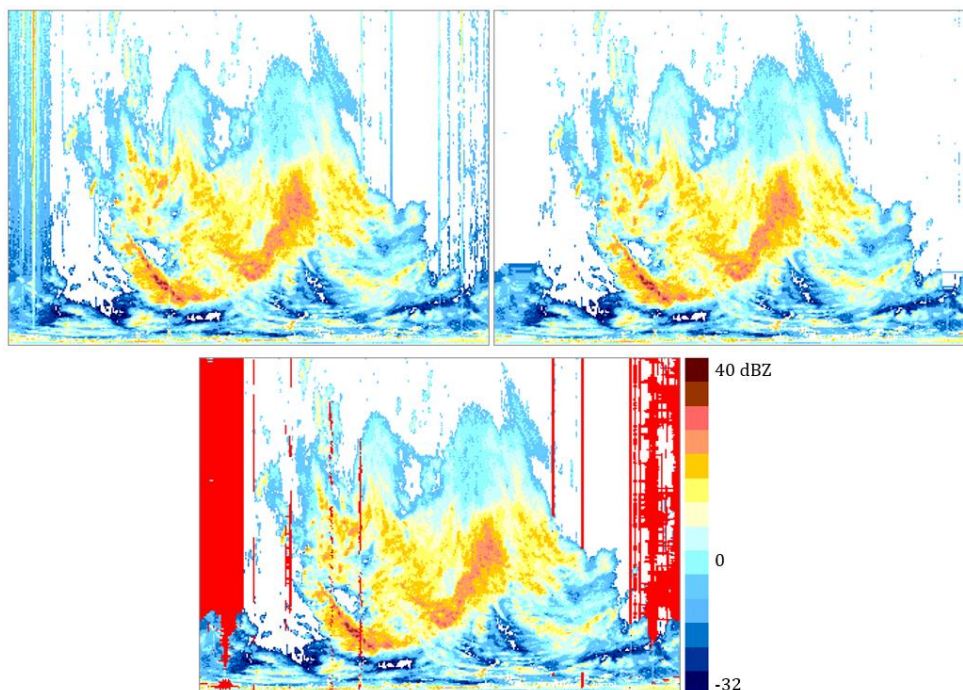
395 *Verification of potential spike-type echoes*

396 This SPIKE sub-algorithm plays a verifying role for all the sub-algorithms described above: it is used to check all echoes
397 that have been flagged as “potential” spike echoes, that is, suspected to be non-meteorological echoes.

398 For this aim, in a given azimuth α and elevation ε the number of bins where “potential” spike echoes have been
399 detected is counted separately for each spike echo type. If a pre-set threshold value has been exceeded, the bins with
400 “potential” spikes of all types at a given azimuth α and elevation ε are considered confirmed spikes.

401 An example of detecting spike echoes, including the “wide”, “narrow”, and “inverse”, is shown in Fig. 11. At the
402 locations marked in red (in the bottom figure) where such echoes have been detected, interpolation of the values was
403 performed (see Sect. 5) – the result is shown in the picture on the right.

404



405

406 **Figure 11:** An example of detecting spike echoes with the SPIKE algorithm using sub-algorithms for “wide”, “narrow”, and
407 “inverse” spikes, from the left: raw and corrected data, and at the bottom mask (in red) of detected spike echoes. Gdańsk radar,
408 the lowest elevation, 30 September 2019, 14:00 UTC.

409 *Quality index*

410 The QI_{SPIKE} quality index for individual radar bins, and the whole radar beam in which any type of spike has been detected,
411 is determined from the following formula, in which after fulfilling the first condition in order in the formula, the QI value is
412 decreased and the procedure is stopped:



$$413 \quad QI_{SPIKE}(\varepsilon, \alpha, l) = \begin{cases} 0.2 & \text{the "wide" spike is detected in a bin } (\varepsilon, \alpha, l) \\ 0.7 & \text{the "wide" spike is detected in a beam } l \\ 0.5 & \text{the "narrow" spike is detected in a bin } (\varepsilon, \alpha, l) \\ 0.8 & \text{the "narrow" spike is detected in a beam } l \\ 0.8 & \text{the "shorter longitudinal" spike is detected in a bin } (\varepsilon, \alpha, l) \\ 0.9 & \text{the "shorter longitudinal" spike is detected in a beam } l \\ 0.5 & \text{the "discontinuous" spike is detected in a bin } (\varepsilon, \alpha, l) \\ 0.8 & \text{the "inverse" spike is detected in a beam } l \\ 1.0 & \text{no spike in a beam } l \end{cases} \quad (14)$$

414 4. Correction of detected non-meteorological echoes – INTERP algorithm

415 Non-meteorological echoes detected with the use of specialized algorithms must be replaced with more reliable values of
 416 radar reflectivity. In the RADVOL-QC system this is performed by the INTERP algorithm, which works on radar bins that
 417 have been flagged by the algorithms DP.TURBINE, DP.NMET, TURBINE, and SPIKE as being burdened with non-
 418 meteorological echoes.

419 4.1. Removal of RLAN interference detected by the SPIKE algorithm

420 Values of radar reflectivity flagged as spikes in bins are interpolates in the following way: for a given flagged bin, the bins in
 421 adjacent and then the further azimuths (on the left and right) at the same distance to the radar site are checked until un-
 422 flagged ones are found. Reflectivity value in the analysed bin is determined as an average from both values found on the left
 423 and right, but if one of the interpolating values is “no echo” then interpolated value is taken as “no echo” as well.

424 4.2. Removal of non-meteorological echoes detected by DP.TURBINE, DP.NMET, and TURBINE algorithms

425 Values in radar bins in which non-meteorological echoes have been detected by algorithm DP.TURBINE, DP.NMET, or
 426 TURBINE are spatially interpolated. At the top elevation, echoes in the bins flagged as non-meteorological are removed. At
 427 other elevations, flagged adjacent bins are clustered into objects which are divided into ordinary and large ones using a pre-
 428 set threshold.

429 For ordinary objects the interpolation is performed in the following way: for a particular object at elevation ε two
 430 values are determined – $Z_{out}(\varepsilon)$, the averaged reflectivity in bins closely surrounding the object in a given elevation (ε) and
 431 $Z_{in}(\varepsilon + 1)$, averaged reflectivity from bins corresponding to the position of the object on the neighbouring higher elevation
 432 ($\varepsilon + 1$). The difference c between the two values:

$$433 \quad c = Z_{in}(\varepsilon + 1) - Z_{out}(\varepsilon) \quad (15)$$

434 is employed to retrieve corrected data by subtracting this difference from the disturbed values:

$$435 \quad Z_{cor}(\varepsilon, a, l) = \min\{Z(\varepsilon + 1, a, l) - c, Z(\varepsilon, a, l)\} \quad (16)$$

436 For large objects, the difference c is assumed to be zero, and then Equation 16 takes the simpler form:

$$437 \quad Z_{cor}(\varepsilon, a, l) = \min\{Z(\varepsilon + 1, a, l), Z(\varepsilon, a, l)\} \quad (17)$$

438 5. Verification

439 The verification of the solutions proposed in Section 3 is presented along with the descriptions of individual algorithms,
 440 because the effectiveness of each algorithm should be assessed separately. Moreover, in this Section the verification of the
 441 performance of the complete RADVOL-QC system is presented.

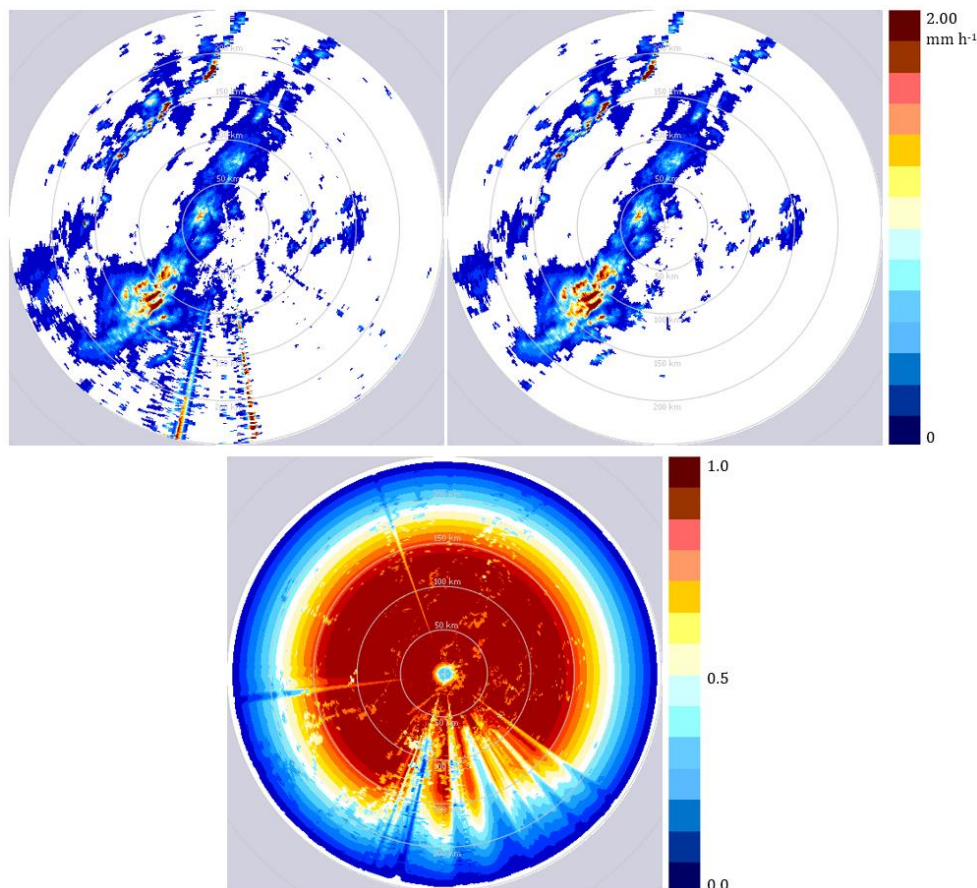


442 The effect of disturbances in weather radar data on the uncertainty of the results of the various meteorological and
443 hydrological models ingesting the data, e.g., in assimilation to mesoscale numerical weather prediction models or as an input
444 to hydrological rainfall-runoff models (Sokol et al., 2021), depends on the specific application. It is difficult to carry out one
445 general verification of the effectiveness of algorithms used to quality control this data.

446 The simplest form of verification is a visual investigation of the effect of corrections on particular time-steps. Fig. 12
447 shows an example of the combined performance of all the algorithms of the RADVOL-QC system. This example is
448 presented in the Cartesian system with the radar site in the centre, as the data from a single radar are usually distributed to
449 applications and end-users in this form. Surface rainfall intensity (SRI) radar product at the height of 1 km above ground
450 level is employed. In this figure for Ramža radar, on the left echoes from the following disturbances are visible: several
451 echoes of various types of spikes mainly to the south of the radar site, echoes from the side lobes near the radar, as well as
452 single non-meteorological echoes observed especially in the eastern part (mainly caused by residential and industrial
453 buildings, hills and wind farms). In the right picture, the complete RADVOL-QC system copes with correcting various
454 disturbances in radar data quite effectively.

455 In the QI field for the same time-step, apart from a reduction in the quality of the spike echoes, there is an evident
456 reduction in the QI values in the south – a result of blocking by the mountains at a distance of about 50 km. In addition,
457 worse quality of measurements is clearly visible with increasing distance from the radar site.

458

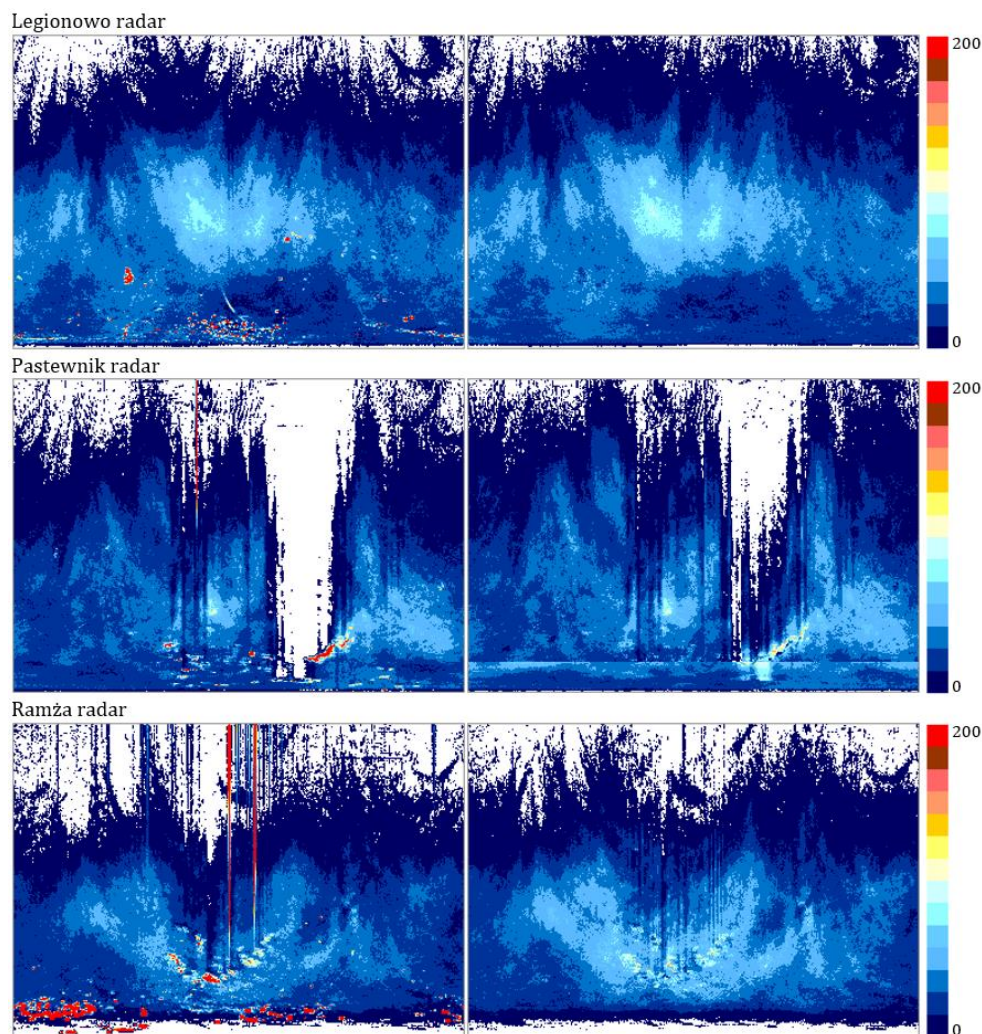


459
460
461

Figure 12: Example of RADVOL-QC algorithm performance, from the left: raw data, data after corrections made with all algorithms, and related quality index field. Ramža radar, SRI product, 2 October 2019, 12:10 UTC, range 250 km.



462 The verification can be performed from the perspective of systems issuing warnings about heavy precipitation. The
463 graphs in Fig. 13 show the number of exceedances of the threshold value of 1 mm / 10 min on the lowest elevation before
464 and after RADVOL-QC corrections over one month; areas with more than 200 alarms are marked in red. It is evident the
465 corrections prevent the generation of false warnings to a large extend.
466



467
468 **Figure 13:** The graphs of the number of exceedances of precipitation 1 mm / 10 min, from the left: raw data and data after
469 corrections (red denotes over 200 exceedances). POLRAD radars: Legionowo, Pastewnik, and Ramża, the lowest elevations,
470 October 2019.

471 All places marked in red can be associated with permanent non-precipitation echoes. These echoes are mainly from
472 mountain areas and large urban centres. For some radars, these are also echoes caused by signals from RLAN antennas
473 (Pastewnik and Ramża radars). The relatively extensive echo visible for the Legionowo radar to the east comes from a large
474 wind farm complex: this is the largest echo from wind turbines visible on the radars of the POLRAD network (see Fig. 8).



475 **6. Conclusions**

476 Over recent years a significant increase in the number of external disturbances in radar measurements has been observed,
477 especially those related to RLAN signals interfering with C-band radar signals, as well as to echoes from turbines and wind
478 farms, because their moving parts affect the radar beam in a specific way. On the other hand, a huge advancement in the
479 technology of radar signal processors used in modern weather radars has been observed – these are much better at filtering
480 out non-meteorological echoes than earlier systems, although the problem is still far from being effectively solved.

481 For these reasons, national meteorological services and various research centres are constantly developing more and
482 more effective algorithms for the detection and removal of non-metrological echoes from radar observations. Software
483 solutions consisting in the analysis of raw 3-D radar data are still an indispensable element of radar data processing systems.
484 Their important feature is that they must be adapted not only to individual types of radars, but also to the local conditions in
485 which they are installed. Algorithms that apply an approach to the problem of eliminating non-meteorological echoes
486 involving the detection and correction of each type of disturbance separately must be constantly developed to take into
487 account their new manifestations.

488 A large part of this study is devoted to such new challenges. This paper does not describe the entire RADVOL-QC
489 system used to quality control data from the Polish weather radar network POLRAD, as it was already published in detail
490 (Ośródko et al., 2014), but only deals with recently introduced new algorithms responding to the increasing importance of
491 various types of disturbances, in particular those resulting from the growing influence of signals from RLAN installations, as
492 well as the impact of wind turbines grouped into large farms.

493 There is no doubt that with the emergence of new sources of disturbance and the intensification of existing ones,
494 sustained work on the development of systems such as RADVOL-QC must be continued in parallel with advances in the
495 technology of radar signal processors.

496 **References**

- 497 Angulo, I., Grande, O., Jenn D., Guerra, D., and de la Vega, D.: Estimating reflectivity values from wind turbines for ana-
498 lyzing the potential impact on weather radar services, *Atmospheric Measurements Techniques*, 8, 2183-2193,
499 doi:10.5194/amt-8-2183-2015, 2015.
- 500 Berenguer, M., Sempere-Torres, D., Corral, C., and Sánchez-Diezma, R.: A fuzzy logic technique for identifying
501 nonprecipitating echoes in radar scans, *J. Atmos. Ocean. Technol.*, 23, 1157–1180, doi:10.1175/JTECH1914.1, 2006.
- 502 Bringi, V. N. and Chandrasekar, V.: *Polarimetric Doppler Weather Radar: Principles and Applications*. Cambridge
503 University Press: Cambridge, UK, ISBN 978-0-521-62384-1, 2001.
- 504 Bringi, V. N., Rico-Ramirez, M. A., and Thurai, M.: Rainfall estimation with an operational polarimetric C-band radar in the
505 United Kingdom: comparison with a gauge network and error analysis, *Journal of Hydrometeorology*, 12, 935–954,
506 doi:10.1175/JHM-D-10-05013.1, 2011.
- 507 Cho, Y.-H., Lee, G. W., Kim, K.-E., and Zawadzki, I.: Identification and removal of ground echoes and anomalous
508 propagation using the characteristics of radar echoes, *J. Atmos. Ocean. Technol.*, 23, 1206–1222,
509 doi:10.1175/JTECH1913.1, 2006.
- 510 Einfalt T., Szturc J., and Ośródko K.: The quality index for radar precipitation data – a tower of Babel? *Atmos. Sci. Lett.*, 11,
511 139-144. doi:10.1002/asl.271, 2010.
- 512 Fornasiero, A., Alberoni, P. P., Amorati, R., and Marsigli, C.: Improving the radar data mosaicking procedure by means of a
513 quality descriptor, 4th European Conference on Radar in Meteorology and Hydrology, Barcelona, Spain, 378-381,
514 2006.



- 515 Gourley, J. J., Tabary, P., and Parent du Chatelet, J.: A Fuzzy logic algorithm for the separation of precipitating from
516 nonprecipitating echoes using polarimetric radar observations, *J. Atmos. Ocean. Technol.*, **24**, 1439–1451,
517 doi:10.1175/JTECH2035.1, 2007.
- 518 Hood, K., Torres, S., and Palmer, R.: Automatic detection of wind turbine clutter for weather radars, *J. Atmos. Ocean.
519 Technol.*, **27**, 1868–1880, doi:10.1175/2010JTECHA1437.1, 2010.
- 520 Isom, B. M., Palmer, R.D., Secrest, G.S., Rhoton, R.D., Saxion, D., Allmon, T.L., Reed, J., Crum, T., and Vogt, R.: Detailed
521 observations of wind turbine clutter with scanning weather radars. *J. Atmos. Ocean. Technol.*, **26**, 894–910,
522 doi:10.1175/2008JTECHA1136.1, 2009.
- 523 Jatho, N., Pluntke, T., Kurbjuhn, C., and Bernhofer, C.: An approach to combine radar and gauge based rainfall data under
524 consideration of their qualities in low mountain ranges of Saxony, *Natural Hazards and Earth System Sciences*, **10**,
525 429–446, doi:10.5194/nhess-10-429-2010, 2010.
- 526 Jurczyk, A., Szturc, J., and Ośródk, K.: Quality-based compositing of weather radar-derived precipitation, *Meteorological
527 Applications*, **27**, e1812, doi:10.1002/met.1812, 2020a.
- 528 Jurczyk, A., Szturc, J., Otop, I., Ośródk, K., and Struzik, P.: Quality-based combination of multi-source precipitation data,
529 *Remote Sens.*, **12**, 1709, doi:10.3390/rs12111709, 2020b.
- 530 Krajewski, W. F., Vignal, B., Seo, B.-C., and Villarini, G.: Statistical model of the range-dependent error in radar-rainfall
531 estimates due to the vertical profile of reflectivity, *J. Hydrol.*, **402**, 306–316, doi:10.1016/j.jhydrol.2011.03.024, 2011.
- 532 Méri, L., Jurašek, M., Kaňák, J., and Okon, E.: Quality-based radar data processing and QPE at the Slovak
533 Hydrometeorological Institute, 10th European Conference on Radar in Meteorology and Hydrology (ERAD 2018),
534 Royal Netherlands Meteorological Institute, Wageningen University, 1–6 July 2018, Ede-Wageningen, The
535 Netherlands, 672–680, doi:10.18174/454537, 2018.
- 536 Méri, L., Gaál, L., Bartok, J., Gažák, M., Gera, M., Jurašek, M., and Kelemen, M.: Improved radar composites and enhanced
537 value of meteorological radar data using different quality indices, *Sustainability*, **13**, 5285, doi:10.3390/su13095285,
538 2021.
- 539 Michelson, D. B., Lewandowski, R., Szewczykowski, M., Beekhuis, H., and Haase, G.: EUMETNET OPERA weather radar
540 information model for implementation with the HDF5 file format, Version 2.2. EUMETNET OPERA Document,
541 2014.
- 542 Michelson, D., Henja, A., Ernes, S., Haase, G., Koistinen, J., Ośródk, K., Peltonen, T., Szewczykowski, M., and Szturc, J.:
543 BALTRAD advanced weather radar networking, *Journal of Open Research Software*, **6**, 12, doi:10.5334/jors.193,
544 2018.
- 545 Norin, L. and Haase, G.: Doppler weather radars and wind turbines, In: J. Bech, J. L. Chau (eds.), *Doppler Radar
546 Observations – Weather Radar, Wind Profiler, Ionospheric Radar, and Other Advanced Applications* (p. 333–354).
547 Rijeka: InTech, ISBN 978-953-51-0496-4, 2012.
- 548 Norin, L.: A quantitative analysis of the impact of wind turbines on operational Doppler weather radar data, *Atmos. Meas.
549 Tech.*, **8**, 593–609, doi:10.5194/amt-8-593-2015, 2015.
- 550 Ośródk, K., Szturc, J., and Jurczyk, A.: Chain of data quality algorithms for 3-D single-polarization radar reflectivity
551 (RADVOL-QC system), *Meteorol. Appl.*, **21**, 256–270, doi:10.1002/met.1323, 2014.
- 552 Ośródk, K. and Szturc, J.: Quality-based generation of weather radar Cartesian products, *Atmospheric Measurement
553 Techniques*, **8**, 2173–2181, doi:10.5194/amt-8-2173-2015, 2015.
- 554 Park, H., Ryzhkov, A. V., Zrníc, D. S., and Kim, K.-E.: The hydrometeor classification algorithm for the polarimetric WSR-
555 88D: description and application to an MCS, *Weather Forecast.*, **24**, 730–748, doi:10.1175/2008WAF2222205.1,
556 2009.



- 557 Peura, M.: Computer vision methods for anomaly removal, 2nd European Conference on Radar Meteorology (ERAD),
558 Proceedings of ERAD 2002, 312-317, 2002.
- 559 Saltikoff, E., Cho, J. Y., Tristant, P., Huuskonen, A., Allmon, L., Cook, R., Becker, E., and Joe, P.: The threat to weather
560 radars by wireless technology, *Bull. Am. Meteorol. Soc.*, 97, 1159-1167, doi:10.1175/BAMS-D-15-00048.1, 2016.
- 561 Saltikoff, E., Haase, G., Delobbe, L., Gaussiat, N., Martet, M., Idziorek, D., Leijnse, H., Novák, P., Lukach, M., and
562 Stephan, K.: OPERA the Radar Project, *Atmosphere*, 10, 320, doi:10.3390/atmos10060320, 2019.
- 563 Sandford, C. and Gaussiat, N.: Use of a radar quality index to mitigate the effects of attenuation at C-band in the UK
564 composite, 7th European Conference on Radar in Meteorology and Hydrology, Toulouse, France, 2012.
- 565 Seo, B.-C., Krajewski, W. F., and Mishra, K. V.: Using the new dual-polarimetric capability of WSR-88D to eliminate
566 anomalous propagation and wind turbine effects in radar-rainfall, *Atmospheric Research*, 153, 296-309,
567 doi:10.1016/j.atmosres.2014.09.004, 2015.
- 568 Sokol, Z., Szturc, J., Orellana-Alvear, J., Popová, J., Jurczyk, A., and Céleri, R.: The role of weather radar in rainfall
569 estimation and its application in meteorological and hydrological modelling – A review, *Remote Sens.*, 13, 351,
570 doi:10.3390/rs13030351, 2021.
- 571 Steiner, M. and Smith, J. A.: Use of three-dimensional reflectivity structure for automated detection and removal of
572 nonprecipitating echoes in radar data, *J. Atmos. Ocean. Technol.*, 19, 673–686, doi:10.1175/1520-
573 0426(2002)019<0673:UOTDRS>2.0.CO;2, 2002.
- 574 Szturc, J., Ośródkka, K., and Jurczyk, A.: Quality control algorithms applied on weather radar reflectivity data, In: J. Bech, J.
575 L. Chau (eds.), *Doppler Radar Observations – Weather Radar, Wind Profiler, Ionospheric Radar, and Other
576 Advanced Applications* (p. 289-306), Rijeka: InTech, ISBN 978-953-51-0496-4, 2012.
- 577 Szturc, J., Jurczyk, A., Ośródkka, K., Wyszogrodzki, A., and Giszterowicz, M.: Precipitation estimation and nowcasting at
578 IMGW (SEiNO system), *Meteorology Hydrology and Water Management*, 6, 3-12, doi:10.26491/mhwm/76120,
579 2018.
- 580 Villarini, G. and Krajewski, W. F.: Review of the different sources of uncertainty in single polarization radar-based estimates
581 of rainfall, *Surv. Geophys.*, 31, 107–129, doi:10.1007/s10712-009-9079-x, 2010.
- 582 Vogt, R. J., Reed, J., Crum, T., Snow, J. T., Palmer, R. D., Isom, B. M., and Burgess, D. W.: Impacts of wind farms on
583 WSR-88D operations and policy considerations, *Preprints, 23rd Int. Conf. on Interactive Information Processing
584 Systems (IIPS) for Meteorology, Oceanography, and Hydrology*, San Antonio, TX. *Amer. Meteor. Soc.*, 5B.7, 2007.
- 585 Zhang, J., Howard, K., Langston, C., Vasiloff, S., Kaney, B., Arthur, A., Cooten, S. V., Kelleher, K., Kitzmiller, D., Ding,
586 F., Seo, D.-J., Wells, E., and Dempsey, C.: National Mosaic and multi-sensor QPE (NMQ) system: description,
587 results, and future plans, *Bull. Am. Meteorol. Soc.*, 92, 1321–1338, doi:10.1175/2011BAMS-D-11-00047.1, 2011.
- 588